Science of the Total Environment 718 (2020) 137267

Contents lists available at ScienceDirect

Science of the Total Environment

journal homepage: www.elsevier.com/locate/scitotenv

Exposure of ultrafine particulate matter causes glutathione redox imbalance in the hippocampus: A neurometabolic susceptibility to Alzheimer's pathology

Soo Jin Park [a,1], Jimin Lee [b,1], Seunghoon Lee [c], Sangchul Lim [c], Juhwan Noh [d,e], So Yeon Cho [b], Junghee Ha [b], Hyunjeong Kim [b], Changsoo Kim [d,e], Sunho Park [c,*], Do Yup Lee [a,**], Eosu Kim [b]

[a] Department of Agricultural Biotechnology, Center for Food and Bioconvergence, Research Institute for Agricultural and Life Sciences, Seoul National University, Seoul, Republic of Korea
[b] Department of Psychiatry, Institute of Behavioral Science in Medicine, BK21 PLUS Project for Medical Sciences, Yonsei University College of Medicine, Seoul, Republic of Korea
[c] Department of Mechanical Engineering, Dankook University, Gyeonggi-do, Yongin, Republic of Korea
[d] Department of Preventive Medicine, Yonsei University College of Medicine, Seoul, Republic of Korea
[e] Institute of Human Complexity and Systems Science, Yonsei University, Seoul, Republic of Korea

HIGHLIGHTS

- Ultrafine particle inhalation causes redox imbalance in the hippocampus.
- Ultrafine particle induces oxidative stress and neuroinflammation.
- Ultrafine particle inhalation increases Alzheimer's beta-amyloid levels.

GRAPHICAL ABSTRACT

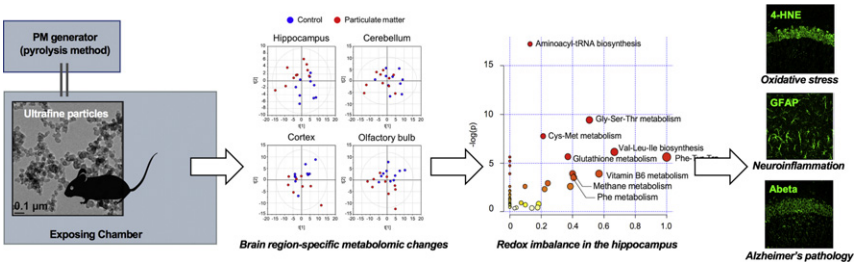

ARTICLE INFO

Article history:
Received 13 August 2019
Received in revised form 7 February 2020
Accepted 10 February 2020
Available online 12 February 2020

Editor: Wei Huang

Keywords:
Ultrafine particle
Alzheimer's disease
Metabolomics
Redox homeostasis

ABSTRACT

Particulate matter (PM) exposure is related to an increased risk of sporadic Alzheimer's disease (AD), the pathogenesis of which is explained by chronic neurometabolic disturbance. Therefore, PM-induced alterations in neurometabolism might herald AD. We aimed to identify brain region-specific changes in metabolic pathways associated with ultrafine particle (UFP) exposure and to determine whether such metabolic alterations are linked to susceptibility to AD. We constructed UFP exposure chambers and generated UFP by the pyrolysis method, which produces no toxic oxidized by-products of combustion, such as NOx and CO. Twenty male C57BL6 mice (11–12 months old) were exposed either to UFP or room air in the chambers for 3 weeks. One week following completion of UFP exposure, regional brain tissues, including the olfactory bulb, cortex, hippocampus, and cerebellum, were obtained and analyzed by metabolomics based on GC–MS and LC-MS, western blot analysis, and immunohistochemistry. Our results demonstrated that the metabolomic phenotype was distinct within the 4 different anatomical regions following UFP exposure. The highest level of metabolic change was identified in the hippocampus, a vulnerable region involved in AD pathogenesis. In this region, one of the key changes was

Abbreviations: 4-HNE, 4-hydroxynonenal; Aβ, β-amyloid; AD, Alzheimer's disease; ATP, adenosine triphosphate; CO, carbon monoxide (CO); CO2, carbon dioxide; FAD, flavin adenine dinucleotide; GC–MS, Gas Chromatography–Mass Spectrometry; GC-TOF MS, gas-chromatography time-of-flight mass spectrometry; GFAP, glial fibrillary acidic protein; HEPA, High-Efficiency Particulate Air; LC-MS, Liquid Chromatography-Mass Spectrometry; LC-Orbitrap MS, Liquid-chromatography Orbitrap mass spectrometry; LOAD, Late-Onset Alzheimer's Disease; O2, oxygen; PCA, principal component analysis; PM, particulate matter; TEM, transmission electron microscope; UFP, ultrafine particle.

* Correspondence to: S. Park, Dankook University, 152 Jukjeon-ro, Gyeonggi-do, Suji-gu, Yongin 16890, Republic of Korea.
** Corresponding to: D.Y. Lee, Seoul National University, 1 Gwanak-ro, Gwanak-gu, Seoul 08826, Republic of Korea.
E-mail addresses: sunhopark@dankook.ac.kr (S. Park), rome73@snu.ac.kr (D.Y. Lee).
[1] These authors contributed equally.

https://doi.org/10.1016/j.scitotenv.2020.137267

Neuroinflammation
Beta-amyloid

perturbed redox homeostasis via alterations in the methionine-glutathione pathway. UFP exposure also induced oxidative stress and neuroinflammation, and importantly, increased Alzheimer's beta-amyloid levels in the hippocampus. These results suggest that inhaled UFP-induced perturbation in hippocampal redox homeostasis has a role in the pathogenesis of AD. Therefore, chronic exposure to UFP should be regarded as a cumulative environmental risk factor for sporadic AD.

1. Introduction

Particulate matter (PM) in ambient air is now well recognized as a crucial risk factor for various illnesses and increased mortality (Brunekreef and Holgate, 2002; Wang et al., 2017; Zhang et al., 2017; Chen et al., 2019). In particular, ultrafine particle (UFP), the size of which is as small as 0.1 μm or even smaller, can enter the circulation through various routes and exert direct toxic effects on multiple organs, including the brain (Li et al., 2003; Chin-Chan et al., 2015). Indeed, several epidemiological and experimental studies have suggested that PM exposure is associated with an increased risk for Alzheimer's disease (AD) (Chin-Chan et al., 2015; Jung et al., 2015; Jang et al., 2018). Although neuroinflammation has been suggested as a mediator of the relationship between PM exposure and AD risk (Calderon-Garciduenas et al., 2008; Block and Calderon-Garciduenas, 2009; Calderon-Garciduenas et al., 2012), how UFP exposure predisposes aged brains to AD has not been fully investigated.

AD, the most common form of aging-related dementias, is a multietiological disease. Only a small portion (<5%) of the disease (familial form of AD) develops from genetic mutations, with onset at a relatively young age (before 65). In contrast, the cause of sporadic, late-onset AD (LOAD), which constitutes >95% of all cases, is still elusive. Deposition of beta-amyloid (Aβ) leading to senile plaques is a hallmark of AD pathology, commonly in both familial and sporadic forms. However, regarding sporadic LOAD, neurometabolic dysfunction has been proposed as a core etiology which may precede Aβ pathology (Buckner et al., 2005; Kang et al., 2017; de la Monte and Tong, 2014). Several key findings have contributed to this metabolic point of view towards LOAD, namely, 'metabolic hypothesis of AD' (Buckner et al., 2005). Firstly, metabolic rate of glucose has been found to be significantly decreased in the brains of patients with LOAD even though all the patients were in normoglycemic state (Hoyer et al., 1991). Consistently, it has been reported that insulin concentration and the activity of insulin receptor are decreased in LOAD brain while the density of insulin receptor is increased (Frolich et al., 1998; Hoyer, 2002). Secondly, it has been revealed that the increased levels of aerobic glycolysis (implicating reduced oxidative phosphorylation) is positively correlated with levels of Aβ deposition in specific brain regions which show default-mode resting state activity in young individuals, suggesting such neurometabolic alteration to be a preceding factor to Aβ pathology in LOAD (Vlassenko et al., 2010). Additionally, various aspects of metabolic impairments in the brain such as redox imbalance, oxidative stress and mitochondrial dysfunction have also been associated with the pathogenesis of LOAD (Sutherland et al., 2013; Birnbaum et al., 2018; Rowland et al., 2018).

Of note, chronic environmental or dietary exposures to toxic substances have been suggested as etiologic factors disrupting brain metabolism (de la Monte et al., 2009; de la Monte and Tong, 2014). For instance, hypercholesterolemia in mid-life has been associated with higher incidence of AD in later life (Kivipelto et al., 2001), and an experimental high-cholesterol diet has shown to cause neuronal metabolic disturbances contributing to LOAD pathogenesis (Wang et al., 2013).

As well as a high-cholesterol diet, UFP should be regarded as a chronic environmental risk factor for AD. Thus, it would be reasonable to investigate the potential contribution of UFP to AD pathogenesis in the context of "neurometabolic vulnerability" in older age. To this end, we conducted an integrative metabolomic analysis based on gas-chromatography time-of-flight mass spectrometry (GC-TOF MS) and liquid-chromatography Orbitrap mass spectrometry (LC-Orbitrap MS). GC–MS, a robust and highly-reproducible analytical platform, is suitable for exploratory and hypothesis-generating research (Cho et al., 2017; Ji et al., 2018), whereas LC-MS is renowned for its broader coverage and high sensitivity upon optimization of target compounds. Thus, this combinatorial approach is ideal for defining overall metabolomic physiology and determining biochemical mechanisms. In addition, we evaluated four different brain regions (hippocampus, cerebellum, cortex, and olfactory bulb) from aged mice exposed to UFP, which allowed for region-specific metabolic responses to UFP from the complex brain matrix to be resolved.

Of note, we applied the "pyrolysis" method to generate UFP without co-production of toxic oxidized by-products, such as nitrogen oxide (NOx) and carbon monoxide (CO), which would have been generated by the "combustion" method; this was to minimize the confounding effects of such toxic chemicals.

2. Methods

2.1. Animals

Male C57BL6/J mice (purchased from the Animal Facilities of Aging Science at Korea Basic Science Institute, Gwangju, South Korea), aged 11–12 months old, were housed under a 12 h light/dark cycle with food and water available ad libitum. All procedures were approved by Yonsei University Institutional Animal Care and Use committee (IACUC-A-201710-640-02) and conformed to the AAALAC (Association for Assessment and Accreditation of Laboratory Animal Care) International guideline (https://www.aaalac.org/resources/Guide_2011.pdf).

2.2. Reagents

Antibodies for western blot analysis and immunohistochemistry were purchased from the companies indicated; GFAP (Glial fibrillary acidic protein; SC-6170, Santa Cruz Biotechnology, Santa Cruz, CA, USA), TNFα (Tumor necrosis factor α; SC-52746, Santa Cruz Biotechnology), β-actin (SC-47778, Santa Cruz Biotechnology), Aβ (6E10) for immunohistochemistry (SIG-39320, Covance, Princeton, NJ, USA), Aβ (B-4) for western blot (SC-28365, Santa Cruz Biotechnology) and 4-hydroxynonenal (4-HNE; AB5605, Millipore, Burlington, MA, USA). LC-MS grade methanol, acetonitrile, water, and ammonium acetate were obtained from Thermo Fisher Scientific (MA, USA). Ammonium hydroxide 25% solution for LC-MS was purchased from Sigma-Aldrich (St. Louis, MO, USA).

2.3. Manufacturing exposure chambers

The exposure chambers were manufactured as illustrated in the schematic (Fig. 1A). The chambers were made of acryl and equipped with a front door, H14 grade HEPA filters on both sides, a ventilation duct on the top, a PM supplying inlet, and sensors for monitoring carbon dioxide (CO_2), oxygen (O_2), and temperature. PM produced by the PM generator was mixed with 99.999% purity air and then supplied to the exposure chamber through the PM supplying inlet.

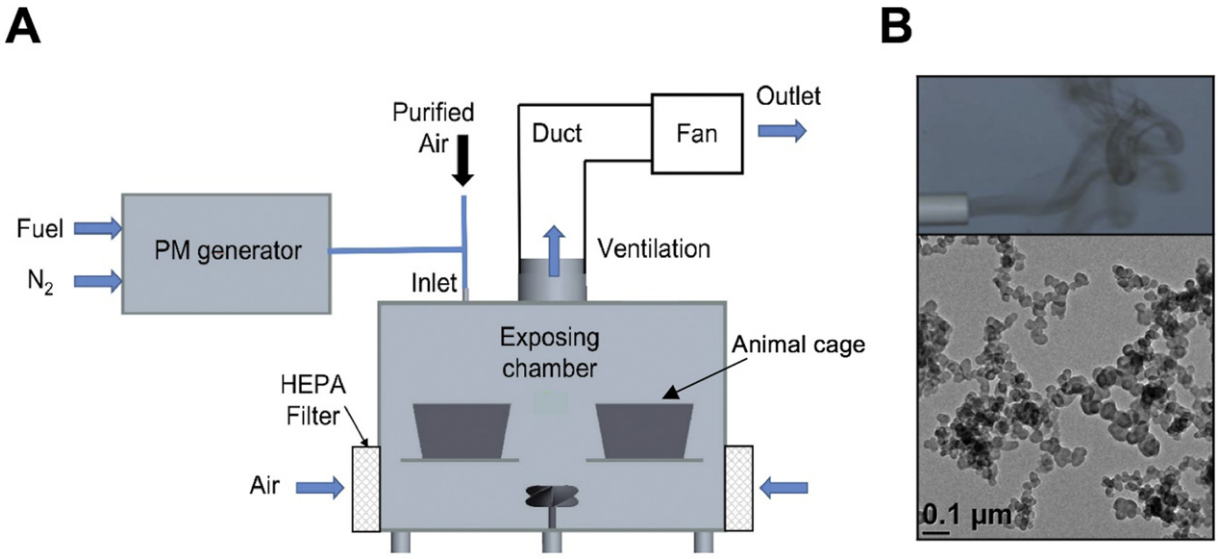

Fig. 1. A schematic of the exposure system. (A) PM generator, exposure chamber, and ventilation systems. Note that two animal cages are put in the chamber. (B) A photo of the PM generator outlet (top) and a TEM image of the PM (bottom) used for the exposure experiment. The average size of primary particles and the aerodynamic size of the agglomerates were 27.4 nm and 178 nm, respectively, corresponding to ultrafine particles (UFP). PM, particulate matter.

2.4. UFP generation and characterization

In general, PM originates from incomplete combustion of fuel. When PM is produced using a flame, its size and chemical composition are difficult to control. In addition, the exhaust gas contains NOx and CO, which are harmful to the human body (Lim et al., 2017). To avoid these problems including the confounding effects of NOx and CO on brain function, we used a PM generator to synthesize UFP by pyrolysis of fuel dispersed in nitrogen (N_2), eliminating the effect of NOx and CO from the UFP exposure experiment. This PM generator was found to produce PM with well-controlled particle characteristics, such as a primary particle size, chemical composition, morphology, and agglomerate size distribution (Cho et al., 2016). The characteristics of this PM have been found to be similar to those of PM emitted from ships, automobile engines, or industrial combustors, depending on the synthesis condition.

Desired particle characteristics were achieved by adjusting the flow rates of the fuel and carrier nitrogen being supplied to the PM generator as well as the temperature of the pyrolysis furnace. A steady flow of propylene (C_3H_6) diluted in nitrogen (fuel mole fraction = 0.01) was pyrolyzed in the furnace at 1300 °C such that PM was continuously generated through nucleation, surface growth, and agglomeration steps.

Fig. 1B shows an image of the PM generator outlet and a transmission electron microscopy (TEM) image of the synthesized PM, which was sampled with a TEM grid at the exhaust of the PM generator. The PM from the generator always remains aerosolized since its generation from a gaseous fuel. This fact makes it unnecessary to blow and aerosolize powder-type carbon particles that many other studies have utilized to create a PM-suspended atmospheric condition. More examples of PM sampling and TEM imaging can be found in our previous publication (Lee et al., 2019). A PM agglomerate consists of many spherical primary particles. The average primary particle size was 27.4 nm, and the standard deviation was 4.2 nm (Fig. S1A). For this calculation, >200 spherules were randomly chosen from multiple TEM images, and their sizes were measured using ImageJ software (Schneider et al., 2012). In addition, the size distribution of PM agglomerates was achieved using a particle size analyzer (Nanoscan SMPS 3910, TSI, USA), and the average aerodynamic size of the PM was found to be 178 nm and the standard deviation was 65 nm (Fig. S1B). Therefore, we assumed that most of the particles (ranging from primary particles to agglomerates) used in this study correspond to UFP.

In general, PM generated by combustion or pyrolysis of pure hydrocarbons consists of crystallized graphitic elemental carbon (EC) and amorphous OC (organic carbon). The organic mass fraction, which is defined by the mass of OC in PM divided by the total mass of PM, was measured using a combustion type particulate analyzer (MEXA-1370PM, Horiba, Japan). The device measures the masses of EC and OC separately by utilizing the difference between EC and OC in their volatility and oxidation behaviour (Lee et al., 2019; Lim et al., 2017). In this study, the PM organic mass fraction was about 0.27 and the standard deviation of the repeated measurement results was 0.04.

2.5. UFP exposure

The exposure experiment was performed for 3 weeks following a routine of 5 days per week and 8 h per day while considering a general human activity cycle. The UFP concentration in the exposure chamber was monitored every 20 min using the particle size analyzer to keep >90% of the target concentration, which was set at 1000 μg/m^3. In addition, since the concentration of CO_2 in the chamber is increased by the animals' respiration, the ventilation duct on the top was used for suction with the covers of the HEPA filters when the CO_2 concentration exceeded ~1500 ppm. Once the CO_2 concentration decreased to the desired concentration, UFP was supplied again to raise the UFP concentration to the target value. The main experimental parameters measured during the experiment are summarized in Table S1.

2.6. Brain tissue preparation

Upon completion of the exposure experiment, regional brain tissues were collected after the 7-day stabilization period, which was performed to minimize the acute effects of UFP exposure on brain metabolism during the last session. The mice were anesthetized with the general inhalation anesthetic isoflurane (approximately 1.5–2.0%) and sacrificed by decapitation under sterile conditions. Brains were carefully removed after the skull was opened and dissected. For metabolomics and western blot analyses, the hippocampus, cerebellum, cortex, and olfactory bulb were immediately dissected on ice and frozen at −70 °C. For immunohistochemistry, brain hemispheres were immediately

fixed using 3.7% formaldehyde-containing phosphate buffered saline (PBS). All procedures from decapitation to the freezing of tissues were completed within 8 min consistently across all animals.

2.7. Metabolite extraction from brain tissue samples

Tissue samples were freeze-dried in 2.0 ml tube and disrupted with a single 5-mm steel ball using the Mixer Mill MM400 (Retsch GmbH & Co., Germany). Pulverized samples were extracted with 1.4 ml of a cold methanol-water (9:5, v/v) mixture (Lee and Fiehn, 2008; Bajad and Shulaev, 2011). The mixtures were kept on ice for 15 min and sonicated for 15 min followed by 5-min centrifugation at 14,000*g* and 4 °C. The resulting supernatants were transferred to a new 1.5 ml tube (700 μl for GC-TOF MS and 550 μl for LC-Orbitrap MS). The aliquots were evaporated to dryness in a speed vacuum concentrator (SCANVAC, Korea), and dried extracts were stored at −80 °C until mass spectrometry analysis.

2.8. Metabolite extraction from blood serum samples

Blood serum samples were thawed on ice at 4 °C and 45 μl was aliquoted. An aliquot of serum samples was extracted with 1400 μl of extraction solvent (methanol: water, 9:5, v/v/v). The mixtures were mixed using the Mixer Mill MM400, kept on ice for 15 min, sonicated for 15 min, and centrifuged for 5 min (14,000 g and 4 °C). The supernatants were transferred to a new 1.5 ml tube (700 μl for GC-TOF MS and 670 μl for LC-Orbitrap MS) and concentrated in a speed vacuum concentrator (SCANVAC, Korea). Dried extracts were stored at −80 °C until mass spectrometry.

2.9. Gas chromatography-time-of-flight mass spectrometry

All analytical procedures were performed in a random order to minimize potential systematic error. Dried extracts were methoximated with 5 μl of 40 mg/ml methoxyamine hydrochloride (Sigma-Aldrich, St. Louis, MO, USA) dissolved in pyridine (Thermo, USA), and then incubated for 90 min (800 rpm and 30 °C). For trimethylsilylation, 45 μl of *N*-methyl-*N*-trimethylsilyltrifluoroacetamide (MSTFA +1% TMCS; Thermo, USA) was added to the derivatives and reacted for 60 min at 800 rpm (37 °C). A mixture (2 μl) of 13 fatty acid methyl esters was used for internal retention index (RI) markers, which included C8, C9, C10, C12, C14, C16, C18, C20, C22, C24, C26, C28, and C30 in chloroform (Ji et al., 2018; Lee et al., 2019).

The derivatized metabolites were analyzed with an Agilent 7890B gas chromatograph (Agilent Technologies) coupled to a Leco Pegasus HT time of flight mass spectrometer (LECO, St. Joseph, MI, USA). The 0.5 μl aliquots of the metabolites were injected into an RTX-5Sil MS column (Restek, Gellefonte, PA, USA) controlled by an Agilent 7693 ALS (Agilent Technologies, Wilmington, DE, USA). The initial GC oven temperature was set to 50 °C and held for 1 min. Then, the GC oven temperature was increased by 20 °C/min to 330 °C and held constant for 5 min. Transfer line and ion source temperatures were set to 280 °C and 250 °C, respectively. The mass spectra were acquired ranging from 85 to 500 *m/z* at a scan rate of 20 spectra/s (Park et al., 2019).

ChromaTOF software was used for data acquisition and preprocessing. Results were stored as ChromaTOF-specific Pegasus files (.peg), which included peak apex mass values, complete spectrum with absolute intensities, retention time, peak purity, noise, and signal-to-noise ratio. ChromaTOF-specific peg files were converted to generic text (.txt) files and generic netCDF files for further data evaluation. The text files were exported to a data server with absolute spectra intensities, and further processed using the BinBase algorithm (Kind et al., 2009; Skogerson et al., 2011).

2.10. Liquid chromatography Orbitrap mass spectrometry

The dried samples were re-constituted with 50 μl of 70% acetonitrile for LC-MS. Chromatographic separation was performed on an Ultimate-3000 UPLC system (Thermo Fisher Scientific, USA) and a 150 × 2.1 mm UPLC BEH 1.7-μm HILIC column (Waters, USA) equipped with 5.0 mm × 2.1 mm UPLC BEH 1.7 μm HILIC VanGuard pre-column (Waters, USA). The mobile phase consisted of buffer A (19 mM ammonium acetate and 68 mM ammonium hydroxide in 5% acetonitrile) and buffer B (100% acetonitrile). The flow rate was set to 0.3 ml/min and a gradient was programmed as follows: 0 min, 95% B; 10 min, 85% B; 20 min, 10% B; 25.1–30 min, 95% B.

Mass-spectrometric analysis was performed on a Q-Exactive plus instrument (Thermo Fisher Scientific, MA, USA) with positive ionization mode for all detections. The acquisition method was conducted using a combination of the two-scan mode, Full MS and targeted SIM (tSIM)-data dependent MS/MS (ddMS2). The Full MS scan ranged from 100 to 1500 *m/z*, and the tSIM-ddMS2 scan mode was applied for acetyl-CoA (810.1316 *m/z*, 14.5–15.6 min), nicotinamide adenine dinucleotide (NADH; 666.1285 *m/z*, 14.1–15.1 min), nicotinamide adenine dinucleotide phosphate (NADPH; 746.0979 *m/z*, 14–15 min), malonyl-CoA (854.1229 *m/z*, 14.8–15.8 min). Full MS-ddMS2 was performed to annotate un-targeted compounds. Data acquisition and preprocessing were managed using Xcalibur software (Thermo Fisher Scientific, San José, CA, USA). RAW data files were processed using Compound Discoverer 2.0 software (Thermo Fisher Scientific, San José, CA, USA). Compound annotation was performed against mzCloud node in which the MS2 mass tolerance and annotation threshold were set to 10 ppm and 70, respectively.

2.11. Cell viability assay

Apoptotic nuclear DNA breaks in the tissue sections were assessed by double fluorescent labeling using a terminal dUTP nick-end labeling (TUNEL) assay (11684795910, Sigma-Aldrich Co.) and 4, 6-diamidino-2-phenylindole (DAPI, Sigma-Aldrich Co.). Brain hemisphere sections (20 μm-thick) were air-dried at room temperature, and permeabilized in PBS with 0.3% Triton X-100 for 1 h. Positive control sections were incubated with a proteinase K working solution (20 μg/ml) for 30 min. Then, sections were incubated with reaction mixtures for 60 min at 37 °C in a humidified atmosphere in the dark. Sections were washed three times with PBS and counter-stained with DAPI (Sigma-Aldrich Co.)

2.12. Western blot analysis

Brain tissues from the different regions (cortex, hippocampus, olfactory bulb, and cerebellum) were homogenized with lysis buffer containing 20 mM HEPES (pH 7.0), 1 mM EGTA, 10 mM KCl, 1.5 mM MgCl2, 250 mM sucrose, and cocktails of phosphatase inhibitors and protease inhibitors at a concentration of 10 μl per 1 mg wet weight of frozen brain tissue. Homogenates were incubated for 10 min on ice with gentle rocking, and then samples were centrifuged at 8000*g* for 30 min at 4 °C. Proteins were resolved on gradient sodium dodecyl sulfate (SDS)-polyacrylamide gels and blotted onto polyvinylidene fluoride (PVDF) membranes (10,600,023, Amersham Biosciences, Piscataway, NJ, USA). Membranes were washed with tris-buffered saline tween-20 (TBS-T; 50 mM Tris/HCl, 140 mM NaCl, pH 7.3, containing 0.1% Tween-20) before blocking non-specific binding with TBS-T plus 3% skimmed milk for 1 h. After blocking, membranes were incubated with the following primary antibodies overnight 4 °C: 4-HNE for oxidative stress (1:3000), TNFα for neuroinflammation (1:2000), Aβ(B-4) for AD pathology (1:1000) in 3% skimmed milk plus TBST-T. After washing, blots were incubated with secondary antibodies conjugated with horseradish peroxidase (1:5000) for 1 h, followed by enhanced

chemiluminescence (Amersham ECL Select Western Blotting Detection Reagent, RPN2235, Amersham Biosciences, Piscataway, NJ, USA) detection.

2.13. Immunohistochemistry

Fixed frozen hemispheres were cut into 20 μm coronal sections using a cryostat. Sections were permeabilized in PBS with 0.3% Triton X-100 for 1 h, and stained in floating condition. Sections were blocked using 5% bovine serum albumin (BSA) in PBS with 0.3% Triton X-100 for 1 h. After blocking, sections were incubated with anti-4-HNE-antibody (1:300), anti-GFAP-antibody (1:500) or anti-Aβ(6E10)-antibody in PBS containing 2% BSA and 0.3% Triton X-100 at 4 °C overnight. After washing with PBS three times, slices were labeled with secondary antibodies (1:500) targeting donkey anti-goat IgG conjugated to Alexa-488 (705–545-003, Jackson ImmunoResearch Laboratories, West Grove, PA, USA) for 1 h. Sections were washed three times with PBS. Sections were counter-stained with DAPI (Sigma-Aldrich Co., St. Louis, MO, USA) and observed under a confocal laser scanning microscope (Carl Zeiss, Thornwood, NY, USA).

2.14. Statistical analyses

Statistical analyses were performed on all continuous variables acquired from the GC–MS and LC-MS. Datasets were normalized using the "MS total useful signal" (MSTUS) approach (NOREVA, http://idrb.zju.edu.cn/noreva/) (Li et al., 2017). Unsupervised multivariate statistics (principal component analysis, PCA) was performed on UV-scaled data by SIMCA 14 (Umetrics AB, Umea, Sweden). A Student's *t*-test was performed to calculate p-values using Microsoft Excel (Microsoft, Seattle, WA, USA). Some graphs were produced using Prism 8 (GraphPad Software, San Diego, CA, USA). Multi Experimental Viewer (MeV, TIGR) was applied to estimate false discovery rate (FDR) and compute q-values. The significance level was set at $\alpha = 0.05$. The metabolite-disease network was constructed using Network Explorer module, and pathway over-representation analysis was applied based on the hypergeometric test and relative-betweenness centrality implemented in MetaboAnalyst 4.0 (Chong et al., 2018). The metabolic network was generated based on a chemical structure similarity and reaction pair information (Barupal et al., 2012) and visualized by a prefuse force-directed layout using Cytoscape 3.7.1 (Shannon et al., 2003).

3. Results

3.1. Perturbed metabolomic phenotypes in the brain upon UFP exposure

First, untargeted metabolite profiling based on GC-TOF MS was conducted on mouse brain tissue, which resulted in 110 structurally identified compounds, and covered a range of central carbon/nitrogen metabolism. The metabolomic phenotype was primarily distinctive according to the different anatomical regions (hippocampus, cerebellum, cortex, and olfactory bulb; Fig. 2A). Score scatter plots from unsupervised multivariate statistics (PCA) indicated the relative similarity between the hippocampus and olfactory bulb. Next to the brain regional heterogeneity, the metabolic profiles were clearly discriminated by UFP exposure, in particular the hippocampus relative to other brain regions (Fig. 2B).

Subsequent univariate statistics verified the highest level of metabolic changes in the hippocampus following UFP exposure (31 metabolites, p-value < 0.05; 21 metabolites, FDR q < 0.001). Most of the

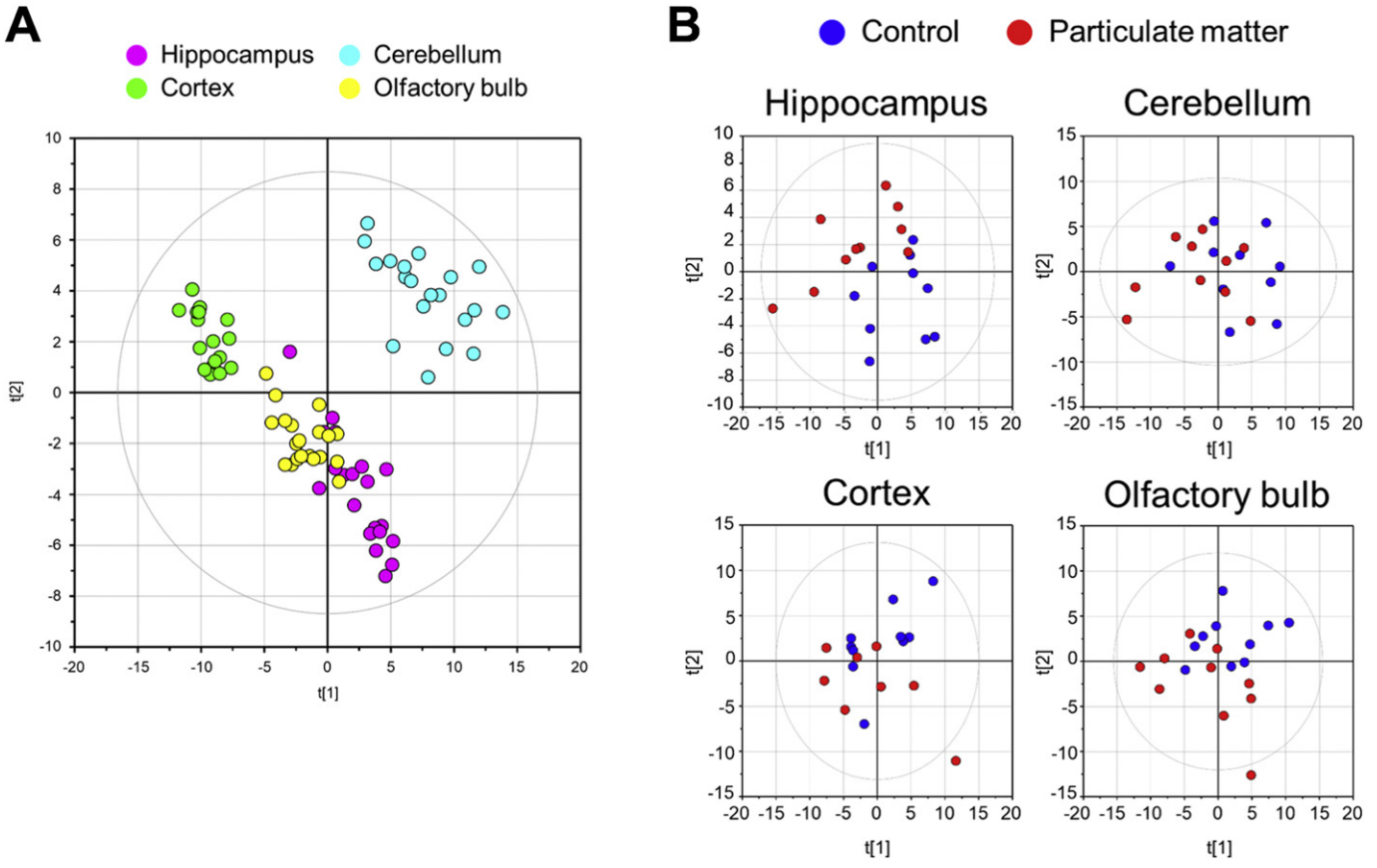

Fig. 2. Distinctive metabolic physiology based on unsupervised multivariate statistics (PCA) by brain-regional specificity (A) and by PM (UFP) exposure in each brain region (B). The metabolite profiles are mainly discriminated according to different regions (A). Hippocampus present the most distinctive clusters between the PM group and controls compared to the other brain regions (B).

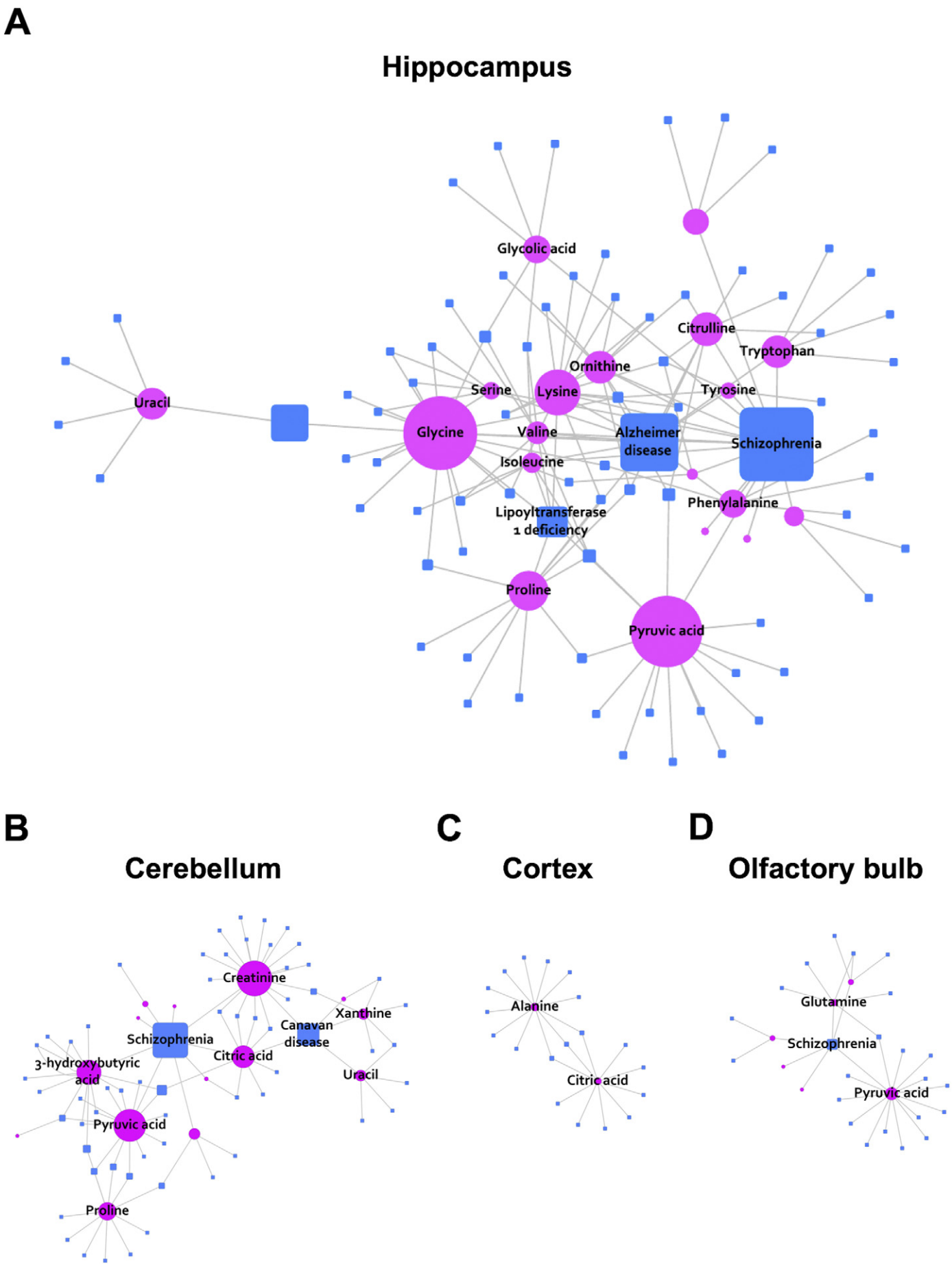
A
Hippocampus
Glycolic acid
Citrulline
Tryptophan
Ornithine
Serine
Lysine
Tyrosine
Uracil
Glycine
Valine
Alzheimer disease
Schizophrenia
Isoleucine
Phenylalanine
Lipoyltransferase 1 deficiency
Proline
Pyruvic acid
B
Cerebellum
Creatinine
Xanthine
Canavan disease
Schizophrenia
Citric acid
3-hydroxybutyric acid
Uracil
Pyruvic acid
Proline
C
Cortex
Alanine
Citric acid
D
Olfactory bulb
Glutamine
Schizophrenia
Pyruvic acid

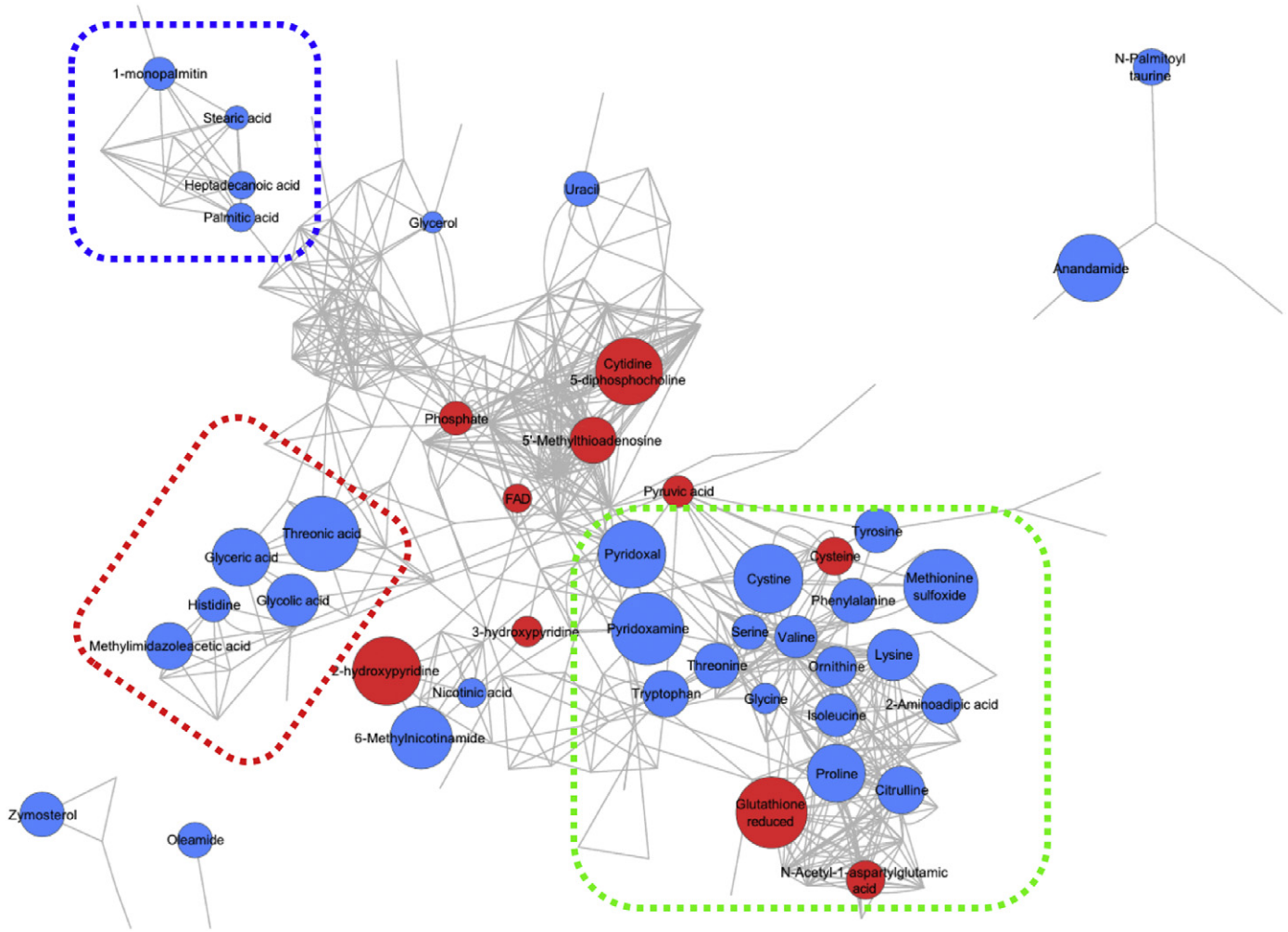

Fig. 4. Identification of key metabolic module based on reconstructed metabolic network in the hippocampus. The metabolic network was re-constructed based on chemical structural similarity and Kegg reaction pair, which resulted in 4 distinct clusters. Red and blue colors represent the metabolites with significant up- and down-regulation in the PM (UFP) group compared to the controls. Node size is proportional to fold change (PM group/control). Metabolites that were not significantly different were removed for visual clarity. The list of all metabolites is available in the supplementary information.

metabolites were significantly down-regulated (25 compounds out of 31) in the hippocampus. Threonic acid and methionine sulfoxide showed the highest levels of reduction (up to 28%), generally consistent with changes in the other regions, except the cortex. Likewise, 2-hydroxypyridine and 5′-methylthioadenosine presented the most dramatic increases, particularly in the hippocampus and cerebellum. Among the hippocampus-specific metabolites were cysteine, phosphate, glyceric acid, and glycolic acid, which were the most significantly changed by UFP exposure (Fig. S2). In the cerebellum, 11 compounds showed specific changes, including adenosine monophosphate, malic acid, and creatinine, whereas 14 and 5 metabolites were specific to the olfactory bulb and cortex, respectively. Of note, the dysregulated metabolites in the hippocampus (31 metabolites) presented strong connectivity to disease (Fig. 3A). In the metabolite-disease interaction network, AD showed the highest levels of degree and betweenness along with 12 metabolites that were significantly altered in the hippocampus. This contrasted with the other brain regions. In the cerebellum and olfactory bulb, schizophrenia was connected to 9 and 5 metabolites, respectively (Fig. 3B, D). The cortex showed no enriched connectivity between disease and metabolites ($n < 5$) (Fig. 3C).

3.2. Hippocampal redox imbalance as metabolic susceptibility

To detail the metabolic linkage to the potential pathomechanisms, extended-target metabolite profiling using LC-MS was conducted focusing on metabolites related to bioenergetics and redox balance. The primary target was set to 23 metabolites (e.g., adenosine triphosphate (ATP), NADH, NADPH, acetyl-CoA, and glutathione). Seventy-seven compounds were additionally determined that were not detected by GC–MS. The list of metabolites that showed statistically significant differences is available in Table S2. We applied an integrated metabolic network (MetaMapp), which systematically binned metabolites according to chemical structural similarity and Kegg reaction pair (Lee et al., 2012; Lee et al., 2016; Park et al., 2016; Polyzos et al., 2019). The resulting network effectively depicted a group of metabolites dysregulated by UFP exposure (Fig. 4). Primarily, coincident down-regulation

Fig. 3. Metabolite-disease network of the hippocampus. A metabolite-disease interaction matrix was computed based on Network Explorer implemented in MetaboAnalyst. Circles indicate metabolites and squares indicate disease. Node size presents betweenness. Only node (degree >5) is visualized in the network. Edge is generated based on the metabolite-disease interaction database (MetPriCNet). The metabolite-disease interaction network of hippocampus (A) presented significant association between metabolites and diseases (Alzheimer's disease) compared to the networks of cerebellum (B), cortex (C), and olfactory bulb (D). See more details in the result part.

A

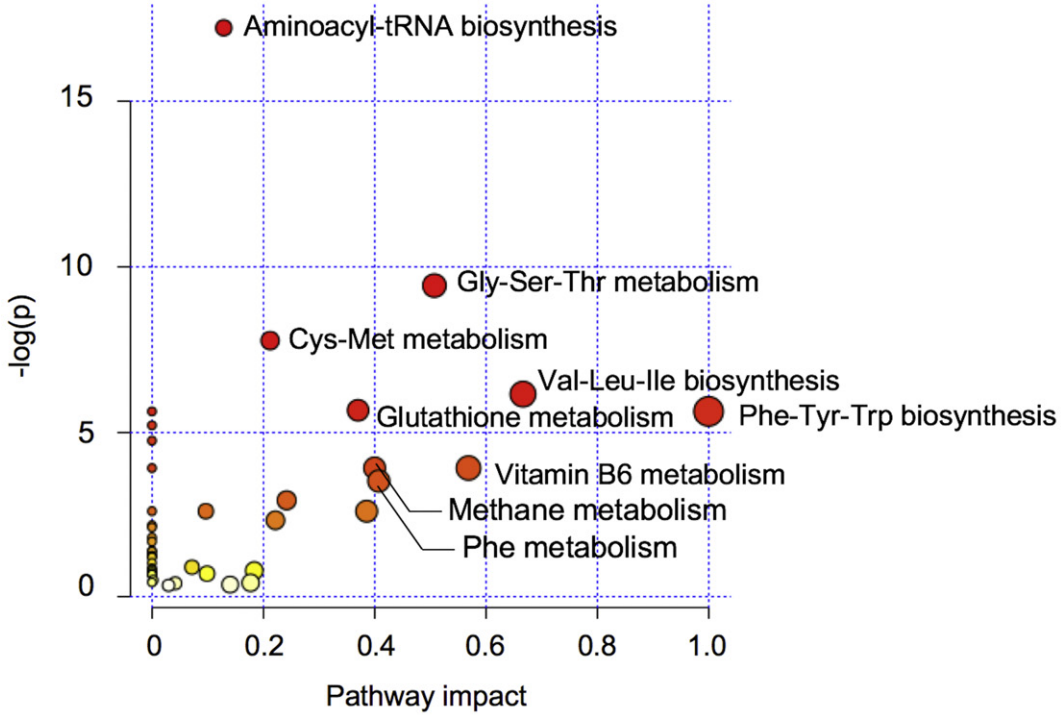
Aminoacyl-tRNA biosynthesis
Gly-Ser-Thr metabolism
Cys-Met metabolism
Val-Leu-Ile biosynthesis
Glutathione metabolism
Phe-Tyr-Trp biosynthesis
Vitamin B6 metabolism
Methane metabolism
Phe metabolism
-log(p)
Pathway impact
15
10
5
0
0
0.2
0.4
0.6
0.8
1.0

B

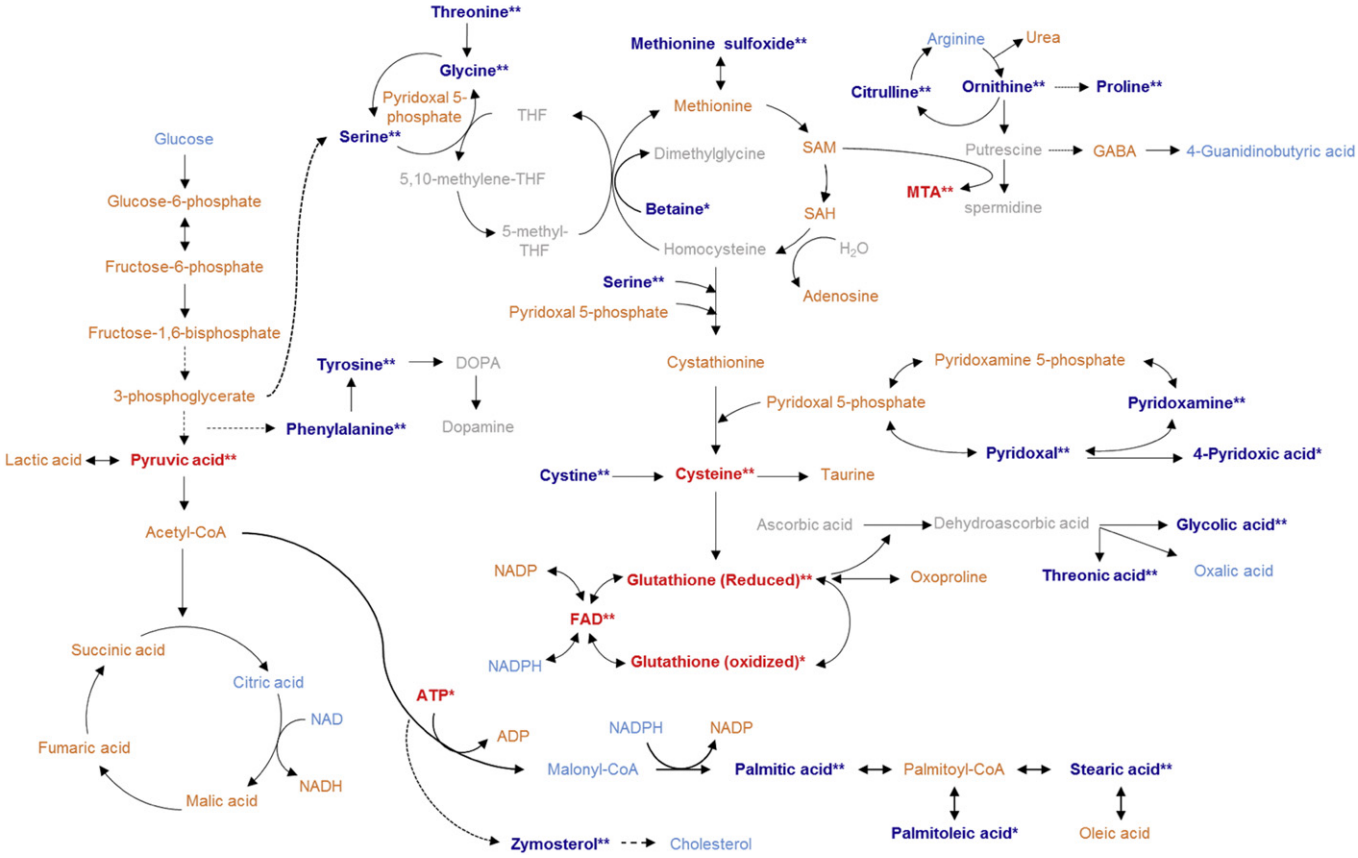
Threonine**
Glycine**
Pyridoxal 5-phosphate
THF
Serine**
5,10-methylene-THF
5-methyl-THF
Glucose
Glucose-6-phosphate
Fructose-6-phosphate
Fructose-1,6-bisphosphate
3-phosphoglycerate
Lactic acid
Pyruvic acid**
Acetyl-CoA
Succinic acid
Citric acid
Fumaric acid
Malic acid
NAD
NADH
Methionine sulfoxide**
Methionine
Dimethylglycine
Betaine*
Homocysteine
SAM
SAH
H2O
Adenosine
MTA**
Arginine
Urea
Citrulline**
Ornithine**
Proline**
Putrescine
GABA
4-Guanidinobutyric acid
spermidine
Serine**
Pyridoxal 5-phosphate
Cystathionine
Tyrosine**
DOPA
Dopamine
Phenylalanine**
Pyridoxamine 5-phosphate
Pyridoxal 5-phosphate
Pyridoxamine**
Pyridoxal**
4-Pyridoxic acid*
Cystine**
Cysteine**
Taurine
Ascorbic acid
Dehydroascorbic acid
Glycolic acid**
Threonic acid**
Oxalic acid
NADP
Glutathione (Reduced)**
Oxoproline
FAD**
NADPH
Glutathione (oxidized)*
ATP*
ADP
NADPH
NADP
Malonyl-CoA
Palmitic acid**
Palmitoyl-CoA
Stearic acid**
Palmitoleic acid*
Oleic acid
Zymosterol**
Cholesterol

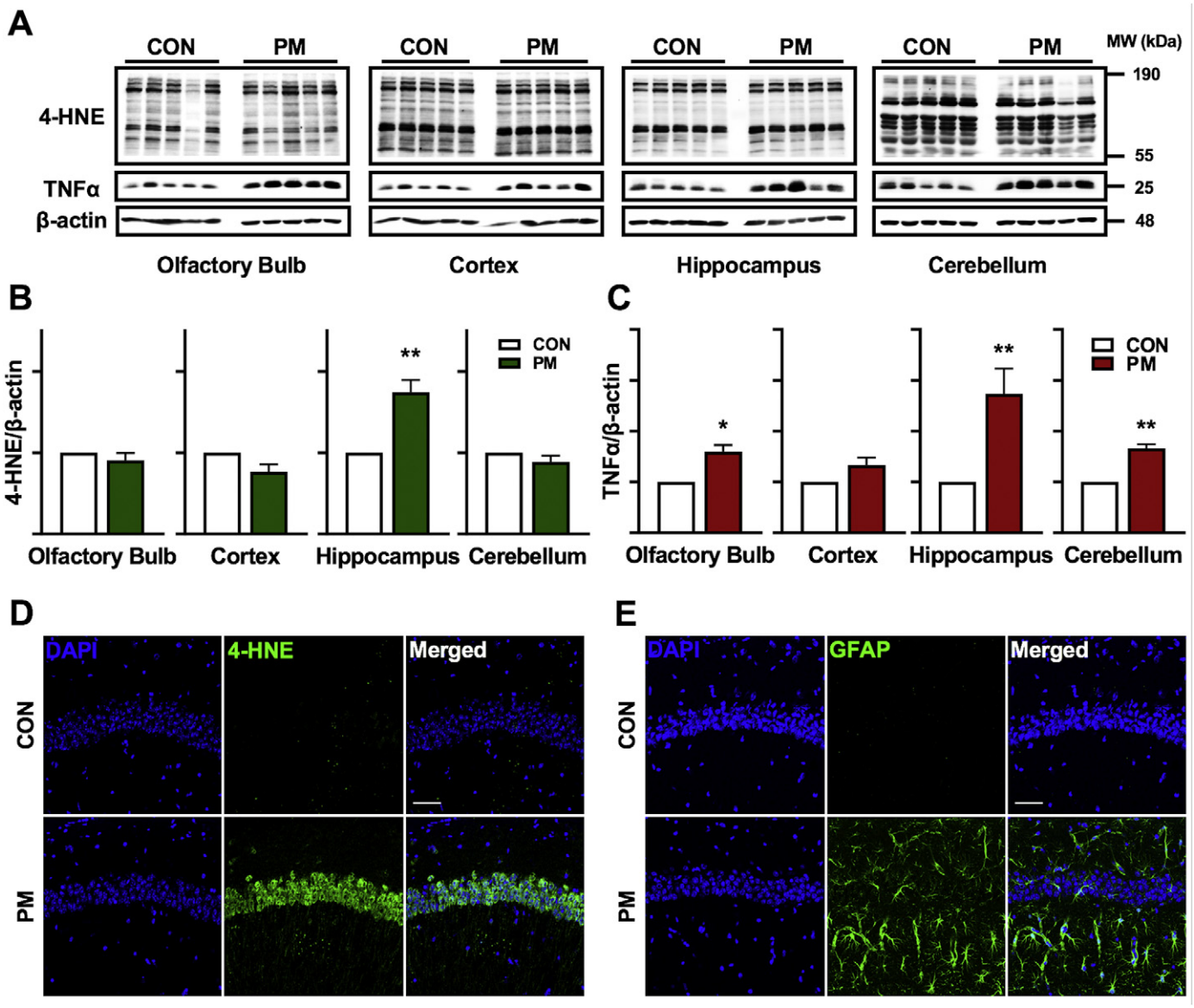

Fig. 6. Oxidative stress and neuroinflammation upon PM (UFP) exposure. (A) Western blot analysis of 4-HNE and TNF-α expression from the olfactory bulb, cortex, hippocampus, and cerebellum (n = 5/group). Equal amounts of protein (20 μg) from lysates from each brain region were used. (B, C) Quantification of western blot band intensity. Data were normalized to β-actin and expressed as relative values to control. $^{*}p < 0.05$, $^{**}p < 0.01$, $^{***}p < 0.001$. (D, E) Immunohistochemistry of 4-HNE (D) and GFAP (E) in the CA1 region of the hippocampus. DAPI (Blue) was used for nuclear counterstaining. Scale bar is 50 μm. CON, control unexposed group; PM, particulate matter exposed group; 4-HNE, 4-Hydroxynonenal.

was identified in nitrogen-containing compounds (green box), including a range of amino acids and vitamin B_6 (pyridoxamine and pyridoxal). In addition, a significant reduction in organic acids (red box) and fatty acid (blue box) was found. The most abundant saturated fatty acids in mammals, palmitic acid and stearic acid, showed 20% and 15% reductions, respectively, compared to the control group. Among the up-regulated metabolites, the highest fold-change was observed in the reduced form of glutathione (2.7-fold change). Others were cysteine, *N*-acetylaspartylglutamic acid, pyruvic acid, 5′-methylthioadenosine, flavin adenine dinucleotide (FAD), and cytidine 5′-diphosphate.

The pathway over-representation analysis proposed the most significant alteration at a pathway level (hypergeometric test, y-axis) with high impact score (relative betweenness centrality, x-axis) (Fig. 5A). The hippocampal region was best characterized by the significant alteration of amino acid metabolism following UFP exposure, particularly Gly-Ser-Thr, Cys-Met, Val-Leu-Ile, and glutathione metabolites (Fig. 5A). Consequent mapping onto the relevant pathways provided

Fig. 5. UFP-driven metabolic pathway dysregulation in the hippocampus. (A) Pathway over-representation analysis of metabolites with significant differences ($p < 0.05$) between the PM (UFP) group and controls. Pathway impact (x-axis) and significance levels (y-axis, −log(p)) were calculated based on relative betweenness and hypergeometric test, respectively. The pathway importance and statistical significance are also presented as node size and color intensity, respectively. (B) Schematic overview of the integrative pathway that is dysregulated in the hippocampus by PM (UFP) exposure. Red and blue indicate significant up- and down-regulation ($^{*}p < 0.1$, $^{**}p < 0.05$), whereas orange and blue-sky indicate moderate changes ($p > 0.1$).

an integrative view of the potential pathomechanisms associated with UFP exposure. The methionine salvage pathway (methionine sulfoxide, betaine, and 5′-Deoxy-5′-methylthioadenosine (MTA)) was coordinately altered with the urea cycle (citrulline, ornithine, and proline) and cysteine-glutathione metabolism (cysteine, glutathione, and FAD) (Fig. 5B). The perturbation was further extended to the aberrant activities of vitamin B_6 and vitamin C metabolism. The metabolic alteration implied a potential disturbance in redox balance associated with oxidative stress.

3.3. Marginal alteration in serum metabolite profiles by UFP exposure

Serum metabolite profiles were further interrogated to examine if the metabolic dysregulation was systemic, which consequently instigated secondary effect on brain metabolism. Indeed, merely marginal differences were observed in serum of the UPF-exposed group. Unsupervised multivariate statistics showed indistinct cluster between the UFP-exposed group and controls (Fig. S3A). Likewise, 5% of metabolites were altered by UFP exposure ($p < 0.05$). It was much lower level compared to the metabolite profiles in the hippocampus tissue (21%). Besides, pathway over-representation analysis showed relatively lower statistical significance and pathway impact score (Fig. S3B). The subsequent mapping on the methionine-glutathione metabolism indicated minimal perturbation associated with redox homeostasis and oxidative stress, which was contrast to the one in the hippocampus tissue dramatically altered by UFP exposure (Fig. S3C). These results argue against the possibility of UFP-induced systemic alteration as a primary cause of brain metabolic dysregulation.

3.4. Hippocampal oxidative stress and neuroinflammation upon UFP exposure

To determine if UFP exposure induced neuronal cell death in the brain, we conducted a TUNEL assay with hippocampal tissues of mice. We found no TUNEL-positive cell death in either group (Fig. S4). This indicates that UFP exposure was not sufficiently toxic to induce apoptotic cell death in the hippocampal tissue, ruling out the possibility that metabolomic changes induced by UFP exposure were secondary to cell death.

Upon observing no cell death, we hypothesized that brain redox changes may be related to the oxidative stress or inflammation induced by UFP exposure. To index oxidative stress and neuroinflammation, we measured the levels of 4-HNE (as an oxidative stress marker) and TNF-α (as inflammation marker). We chose TNF-α because it is a pro-inflammatory cytokine known to play a major role in neuroinflammation process (Liddelow et al., 2017) as well as in early stage of AD pathogenesis (Tarkowski et al., 2003).

UFP significantly increased the levels of 4-HNE in the hippocampus (Fig. 6A, B), and also of TNF-α in the olfactory bulb, hippocampus, and cerebellum (Fig. 6A, C).

To corroborate these findings, we conducted immunohistochemical staining for 4-HNE and GFAP in the hippocampal tissues. We found that the expression of 4-HNE was increased upon UFP exposure in the cornu ammonis 1 (CA1) (Fig. 6D), CA3, and dentate gyrus (DG) (Fig. S5) of the hippocampus. Also, the GFAP signal was increased in the hippocampal tissue following UFP exposure, indicating UFP-induced astrocytic activation (Fig. 6E and Fig. S6). As astrocyte activation induced by TNF-α is a primary cause of neuronal death (Liddelow et al., 2017), our findings suggest a possibility that UFP-induced neuroinflammation might be a preceding cause of neurodegeneration (Tarkowski et al., 2003).

3.5. Alzheimer's Aβ levels in the hippocampus upon UFP exposure

Finally, we assessed the level of brain Aβ to see if UFP exposure indeed increases Alzheimer's pathology in old mice. Aβ levels were significantly increased in the hippocampal tissue of mice exposed to UFP compared to that of control mice, but not in other regions of the brain (Fig. 7A,B), indicating again the susceptibility of AD pathogenesis in the hippocampus. Immunohistochemistry also revealed an obvious increase in hippocampal Aβ levels in CA1 (Fig. 7C), CA3 and DG

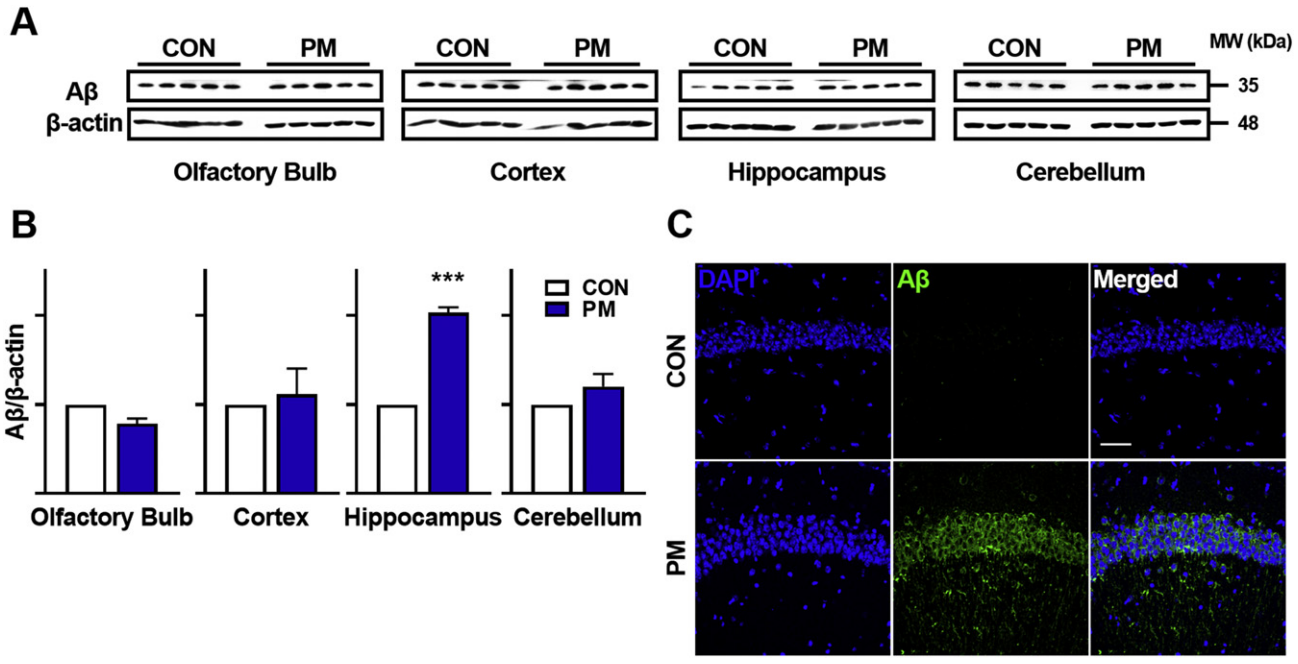

Fig. 7. Increased Aβ levels in the hippocampus upon PM (UFP) exposure. (A) Aβ levels in the cortex and hippocampus were measured by Western blot analysis ($n = 5$/group). Equal amounts of protein (20 μg) from each brain region lysates were used. (B) Quantification of western blot band intensity. Data were normalized to β-actin and expressed as relative values to control. $^{***}p < 0.001$. (C) Immunohistochemistry of Aβ in the CA1 region of the hippocampus. DAPI (Blue) was used for nuclear counterstaining. Scale bar in 50 μm. CON, control unexposed group; PM, particulate matter exposed group.

(Fig. S7). However, apparent changes in Aβ intensity were not observed in other regions of the brain (Fig. S7). This finding suggests that UPF-induced redox imbalance is associated with an increased susceptibility to Alzheimer's pathogenesis.

4. Discussion

To the best of our knowledge, the current study is the first to evaluate region-specific toxicity in the brain following exposure to well-defined UFPs. The comprehensive metabolomic investigation revealed significant UFP-induced perturbations and systematically characterized the regional specificity of the metabolic dysfunction across 4 different brain regions. Among these regions, the most significant changes were found in the hippocampus, one of the first regions to develop pathological signs of AD (Braak and Braak, 1991; Jack et al., 1998). Of note, alterations in this region were best characterized by dysregulated methionine-glutathione metabolism, implying aberrant activity in redox balance. The subsequent molecular examination uncovered evidence of oxidative stress and neuroinflammation in the hippocampus following UFP exposure. Importantly, UFP exposure also caused an increase in the levels of Aβ, a hallmark of Alzheimer's pathology. Therefore, these results collectively suggest the redox imbalance as a metabolic account of the pathogenesis of sporadic LOAD upon UFP exposure.

Neurodegenerative diseases are renowned for region-specific progression of pathologies (Lee et al., 2013). For instance, AD primarily involves the hippocampus, whereas Parkinson's disease and Huntington's disease mainly involve the substantia nigra pars compacta and striatum, respectively. Thus, a spatially-resolved metabolic profile is essential to identify the disease-specificity of UFP-induced alterations. In our current study, we examined 4 different brain regions (hippocampus, cortex, cerebellum, and olfactory bulb). Indeed, UFP significantly affected the primary metabolism in the hippocampus, cerebellum, and olfactory bulb, which implied potential toxicity in a range of areas in the brain. However, hippocampal metabolism was the brain region that showed the most dramatic perturbations, supporting a pathogenic link between UFP exposure and AD susceptibility. Particularly, concomitant alterations in various amino acids were characteristic of the hippocampus. The aberrant activity in amino acid metabolism has been metabolically featured in AD (Gueli and Taibi, 2013; Xu et al., 2016; Griffin and Bradshaw, 2017). The significant down-regulation of aromatic amino acids (tryptophan, tyrosine, and phenylalanine) implies dysfunction in the biosynthetic process for neurotransmitters (Griffin and Bradshaw, 2017; Usuda et al., 2018). Likewise, the reduced levels of branch-chain amino acids (isoleucine and valine) in our current study have been implicated in the cognitive change observed in patients with AD (Toledo et al., 2017). In addition, the urea cycle was moderately differentially increased by UFP, whereas citrulline, ornithine, and proline were significantly lower in the hippocampus of the PM (UFP) group. Dysfunction of urea metabolism has been implicated in AD pathogenesis through defects in osmoregulation or nitrogen metabolism.

The subsequent examination based on extended-target metabolite profiling detailed the putative pathomechanism involved in bioenergetics and redox balance. Primarily, abnormal redox balance was noted, with the highest fold increase in glutathione, a major endogenous antioxidant. Moreover, the moderate level of reduction was determined as the ratio of reduced GSH to its oxidized form ($p = 0.26$; fold change = 0.68), which was consistent with a recent report in an AD mouse model (Zhang et al., 2012). Although glutathione depletion has been generally observed in the postmortem brains from patients with AD, our data imply a systemic dysregulation of the glutathione redox balance. The atypical activity was coupled to the significant increase in FAD, which has been implicated in the pathogenesis of AD in a study of a young transgenic AD mouse using label free fluorescence spectroscopy (Shi et al., 2017). Dysfunction of the glutathione redox cycle was further extended to the methionine salvage pathway and vitamin B_6 metabolism. Notably, recent studies proposed a beneficial effect of B-vitamin supplementation on PM toxicity in a human intervention trial (Zhong et al., 2017a,b).

Additional question was whether the observed metabolomic changes were associated with neuronal death following UFP exposure. We observed no cell death following UFP exposure, as assessed using the TUNEL assay, suggesting UFP exposure was sub-lethal to brain cells. However, consistent with our finding of a glutathione imbalance, we identified significant changes in the levels of 4-HNE and TNF-α, indicating increased oxidative stress and neuroinflammation, respectively (Vassalli, 1992; Poli and Schaur, 2000; Poli et al., 2008). Oxidative stress and neuroinflammation have been regarded as chronic causative factors for AD. Thus, our findings strongly suggest that even a sub-lethal dose of UFP could contribute to AD pathogenesis (such as Aβ) in a chronic and cumulative way. These findings are highly consistent with a recent report showing that PM2.5 causes alterations in glutathione metabolism, energy metabolism, and oxidative/inflammatory cytokines including TNF-α in human lung bronchial epithelial cells (Song et al., 2019).

Although the relationship between PM exposure and AD risk has been consistently suggested, the specific link has been elusive. Accordingly, we performed a strategic experiment to delineate the causality as follows: First, we used the exposure chambers for ecological validity of the inhalation of UFP in ambient air: We used UFP, which penetrates the circulation and the brain (through the brain-blood barrier) and is considered to be more clinically serious than other types of PM (Oberdorster et al., 2004; Brauner et al., 2007). Most importantly, we used the pyrolysis method to generate UFP without co-producing toxic oxidized by-products, such as NOx and CO, which would have also crucially affected brain metabolism. Thus, our results may reflect the effect of UFP, minimizing the secondary (confounding) effects of such toxic chemicals mixed with PM. Second, we used aged mice, which we thought are appropriate for studies to observe UPF-induced pathologies relevant for LOAD. Finally, we had a 7-day stabilization period without UFP exposure before brain tissue sampling to minimize the acute toxic effects of UFP (in the last exposure session).

Several limitations of our study should be addressed. Firstly, we did not directly observe the presence of UFP in the brain tissues. Thus, it remains to be identified whether metabolomic alterations in the brain was direct consequences of UFP deposition in the brain or results of systemic inflammation. However, our finding of metabolome changes in serum and previous evidence that UFP could enter the brain tissue (Oberdorster et al., 2005; Maher et al., 2016) may suggest a direct role of UFP in this tissue rather than systemic inflammation. Secondly, as the primary goal was to detect potentially subtle changes in brain metabolism upon UFP exposure, we did not include experiments examining more severe phenotypes such as behaviour abnormality or various forms of toxic Aβ. (We only measure Aβ42 as a representative form.) Future study should seek evidence of cognitive impairment upon UFP exposure and extensive molecular findings. Thirdly, we did not include female mice to avoid any potential effects of hormonal cycle on neurometabolism. Finally, we applied a 3-week duration of UFP exposure, which could not be generalized to the real-world chronic, cumulative effects of ambient air pollution. Therefore, behavioural experiments with mice of both sexes following chronic exposure of UFP should be a subject of the future study.

5. Conclusions

Our study proposes a link between UFP exposure and the susceptibility to AD using aged mice. In particular, redox imbalance via the methionine-glutathione pathway in the hippocampus was among the most significant findings following UFP exposure. Consistent with these findings on metabolism, increased levels of oxidative stress, neuroinflammation, and Alzheimer's Aβ were also identified in the hippocampus of mice exposed to UFP. These findings suggest that maintaining redox homeostasis could be a practical strategy to

counteract UFP-induced progression in neurodegeneration and reduce the cumulative environmental risk of LOAD.

Declaration of competing interest

The authors declare that they have no known competing financial interests or personal relationships that could have appeared to influence the work reported in this paper.

Acknowledgements

This study was supported by the Korean Ministry of Environment (MOE) as the Environmental Health Action Program (Grant Number 2014001360002) and by the National Research Foundation of Korea (NRF) Grant (NRF-2016R1C1B2007982) funded by the Korean Ministry of Science and ICT.

Appendix A. Supplementary data

Supplementary data to this article can be found online at https://doi.org/10.1016/j.scitotenv.2020.137267.

References

Bajad, S., Shulaev, V., 2011. LC-MS-based metabolomics. Methods Mol. Biol. 708, 213–228. https://doi.org/10.1007/978-1-61737-985-7_13.

Barupal, D.K., Haldiya, P.K., Wohlgemuth, G., Kind, T., Kothari, S.L., Pinkerton, K.E., Fiehn, O., 2012. MetaMapp: mapping and visualizing metabolomic data by integrating information from biochemical pathways and chemical and mass spectral similarity. BMC Bioinf. 13, 99. https://doi.org/10.1186/1471-2105-13-99.

Birnbaum, J.H., Wanner, D., Gietl, A.F., Saake, A., Kundig, T.M., Hock, C., Nitsch, R.M., Tackenberg, C., 2018. Oxidative stress and altered mitochondrial protein expression in the absence of amyloid-beta and tau pathology in iPSC-derived neurons from sporadic Alzheimer's disease patients. Stem Cell Res. 27, 121–130. https://doi.org/10.1016/j.scr.2018.01.019.

Block, M.L., Calderon-Garciduenas, L., 2009. Air pollution: mechanisms of neuroinflammation and CNS disease. Trends Neurosci. 32 (9), 506–516. https://doi.org/10.1016/j.tins.2009.05.009.

Braak, H., Braak, E., 1991. Neuropathological stageing of Alzheimer-related changes. Acta Neuropathol. 82 (4), 239–259. https://doi.org/10.1007/BF00308809.

Brauner, E.V., Forchhammer, L., Moller, P., Simonsen, J., Glasius, M., Wahlin, P., Raaschou-Nielsen, O., Loft, S., 2007. Exposure to ultrafine particles from ambient air and oxidative stress-induced DNA damage. Environ. Health Perspect. 115 (8), 1177–1182. https://doi.org/10.1289/ehp.9984.

Brunekreef, B., Holgate, S.T., 2002. Air pollution and health. Lancet 360 (9341), 1233–1242. https://doi.org/10.1016/S0140-6736(02)11274-8.

Buckner, R.L., Snyder, A.Z., Shannon, B.J., LaRossa, G., Sachs, R., Fotenos, A.F., Sheline, Y.I., Klunk, W.E., Mathis, C.A., Morris, J.C., Mintun, M.A., 2005. Molecular, structural, and functional characterization of Alzheimer's disease: evidence for a relationship between default activity, amyloid, and memory. J. Neurosci. 25 (34), 7709–7717. https://doi.org/10.1523/JNEUROSCI.2177-05.2005.

Calderon-Garciduenas, L., Solt, A.C., Henriquez-Roldan, C., Torres-Jardon, R., Nuse, B., Herritt, L., Villarreal-Calderon, R., Osnaya, N., Stone, I., Garcia, R., Brooks, D.M., Gonzalez-Maciel, A., Reynoso-Robles, R., Delgado-Chavez, R., Reed, W., 2008. Long-term air pollution exposure is associated with neuroinflammation, an altered innate immune response, disruption of the blood-brain barrier, ultrafine particulate deposition, and accumulation of amyloid beta-42 and alpha-synuclein in children and young adults. Toxicol. Pathol. 36 (2), 289–310. https://doi.org/10.1177/0192623307313011.

Calderon-Garciduenas, L., Kavanaugh, M., Block, M., D'Angiulli, A., Delgado-Chavez, R., Torres-Jardon, R., Gonzalez-Maciel, A., Reynoso-Robles, R., Osnaya, N., Villarreal-Calderon, R., Guo, R., Hua, Z., Zhu, H., Perry, G., Diaz, P., 2012. Neuroinflammation, hyperphosphorylated tau, diffuse amyloid plaques, and down-regulation of the cellular prion protein in air pollution exposed children and young adults. J. Alzheimers Dis. 28 (1), 93–107. https://doi.org/10.3233/JAD-2011-110722.

Chen, R., Yin, P., Meng, X., Wang, L., Liu, C., Niu, Y., Liu, Y., Liu, J., Qi, J., You, J., Kan, H., Zhou, M., 2019. Associations between coarse particulate matter air pollution and cause-specific mortality: a nationwide analysis in 272 Chinese cities. Environ. Health Perspect. 127 (1), 17008. https://doi.org/10.1289/EHP2711.

Chin-Chan, M., Navarro-Yepes, J., Quintanilla-Vega, B., 2015. Environmental pollutants as risk factors for neurodegenerative disorders: Alzheimer and Parkinson diseases. Front. Cell. Neurosci. 9, 124. https://doi.org/10.3389/fncel.2015.00124.

Cho, S., Lee, S., Lee, W., Park, S., 2016. Synthesis of primary-particle-size-tuned soot particles by controlled pyrolysis of hydrocarbon fuels. Energy Fuel 30 (8), 6614–6619. https://doi.org/10.1021/acs.energyfuels.6b01346.

Cho, Y.U., Lee, D., Lee, J.E., Kim, K.H., Lee, D.Y., Jung, Y.C., 2017. Exploratory metabolomics of biomarker identification for the internet gaming disorder in young Korean males. J. Chromatogr. B Analyt. Technol. Biomed. Life Sci. 1057, 24–31. https://doi.org/10.1016/j.jchromb.2017.04.046.

Chong, J., Soufan, O., Li, C., Caraus, I., Li, S., Bourque, G., Wishart, D.S., Xia, J., 2018. MetaboAnalyst 4.0: towards more transparent and integrative metabolomics analysis. Nucleic Acids Res. 46 (W1), W486–W494. https://doi.org/10.1093/nar/gky310.

de la Monte, S.M., Tong, M., 2014. Brain metabolic dysfunction at the core of Alzheimer's disease. Biochem. Pharmacol. 88 (4), 548–559. https://doi.org/10.1016/j.bcp.2013.12.012.

de la Monte, S.M., Neusner, A., Chu, J., Lawton, M., 2009. Epidemilogical trends strongly suggest exposures as etiologic agents in the pathogenesis of sporadic Alzheimer's disease, diabetes mellitus, and non-alcoholic steatohepatitis. J. Alzheimers Dis. 17 (3), 519–529. https://doi.org/10.3233/JAD-2009-1070.

Frolich, L., Blum-Degen, D., Bernstein, H.G., Engelsberger, S., Humrich, J., Laufer, S., Muschner, D., Thalheimer, A., Turk, A., Hoyer, S., Zochling, R., Boissl, K.W., Jellinger, K., Riederer, P., 1998. Brain insulin and insulin receptors in aging and sporadic Alzheimer's disease. J. Neural Transm. (Vienna) 105 (4–5), 423–438. https://doi.org/10.1007/s007020050068.

Griffin, J.W., Bradshaw, P.C., 2017. Amino acid catabolism in Alzheimer's disease brain: friend or foe? Oxidative Med. Cell. Longev. 2017, 5472792. https://doi.org/10.1155/2017/5472792.

Gueli, M.C., Taibi, G., 2013. Alzheimer's disease: amino acid levels and brain metabolic status. Neurol. Sci. 34 (9), 1575–1579. https://doi.org/10.1007/s10072-013-1289-9.

Hoyer, S., 2002. The aging brain. Changes in the neuronal insulin/insulin receptor signal transduction cascade trigger late-onset sporadic Alzheimer disease (SAD). A mini-review. J. Neural Transm. (Vienna) 109 (7–8), 991–1002. https://doi.org/10.1007/s007020200082.

Hoyer, S., Nitsch, R., Oesterreich, K., 1991. Predominant abnormality in cerebral glucose utilization in late-onset dementia of the Alzheimer type: a cross-sectional comparison against advanced late-onset and incipient early-onset cases. J. Neural Transm. Park. Dis. Dement. Sect. 3 (1), 1–14. https://doi.org/10.1007/bf02251132.

Jack Jr., C.R., Petersen, R.C., Xu, Y., O'Brien, P.C., Smith, G.E., Ivnik, R.J., Tangalos, E.G., Kokmen, E., 1998. Rate of medial temporal lobe atrophy in typical aging and Alzheimer's disease. Neurology 51 (4), 993–999. https://doi.org/10.1212/wnl.51.4.993.

Jang, S., Kim, E.W., Zhang, Y., Lee, J., Cho, S.Y., Ha, J., Kim, H., Kim, E., 2018. Particulate matter increases beta-amyloid and activated glial cells in hippocampal tissues of transgenic Alzheimer's mouse: involvement of PARP-1. Biochem. Biophys. Res. Commun. 500 (2), 333–338. https://doi.org/10.1016/j.bbrc.2018.04.068.

Ji, D.Y., Park, S.H., Park, S.J., Kim, K.H., Ku, C.R., Shin, D.Y., Yoon, J.S., Lee, D.Y., Lee, E.J., 2018. Comparative assessment of Graves' disease and main extrathyroidal manifestation, Graves' ophthalmopathy, by non-targeted metabolite profiling of blood and orbital tissue. Sci. Rep. 8 (1), 9262. https://doi.org/10.1038/s41598-018-27600-0.

Jung, C.R., Lin, Y.T., Hwang, B.F., 2015. Ozone, particulate matter, and newly diagnosed Alzheimer's disease: a population-based cohort study in Taiwan. J. Alzheimers Dis. 44 (2), 573–584. https://doi.org/10.3233/JAD-140855.

Kang, S., Lee, Y.H., Lee, J.E., 2017. Metabolism-centric overview of the pathogenesis of Alzheimer's disease. Yonsei Med. J. 58 (3), 479–488. https://doi.org/10.3349/ymj.2017.58.3.479.

Kind, T., Wohlgemuth, G., Lee, D.Y., Lu, Y., Palazoglu, M., Shahbaz, S., Fiehn, O., 2009. FiehnLib: mass spectral and retention index libraries for metabolomics based on quadrupole and time-of-flight gas chromatography/mass spectrometry. Anal. Chem. 81 (24), 10038–10048. https://doi.org/10.1021/ac9019522.

Kivipelto, M., Helkala, E.L., Laakso, M.P., Hanninen, T., Hallikainen, M., Alhainen, K., Soininen, H., Tuomilehto, J., Nissinen, A., 2001. Midlife vascular risk factors and Alzheimer's disease in later life: longitudinal, population based study. BMJ 322 (7300), 1447–1451. https://doi.org/10.1136/bmj.322.7300.1447.

Lee, D.Y., Fiehn, O., 2008. High quality metabolomic data for Chlamydomonas reinhardtii. Plant Methods 4, 7. https://doi.org/10.1186/1746-4811-4-7.

Lee, D.Y., Park, J.J., Barupal, D.K., Fiehn, O., 2012. System response of metabolic networks in Chlamydomonas reinhardtii to total available ammonium. Mol. Cell. Proteomics 11 (10), 973–988. https://doi.org/10.1074/mcp.M111.016733.

Lee, D.Y., Xun, Z., Platt, V., Budworth, H., Canaria, C.A., McMurray, C.T., 2013. Distinct pools of non-glycolytic substrates differentiate brain regions and prime region-specific responses of mitochondria. PLoS One 8 (7), e68831. https://doi.org/10.1371/journal.pone.0068831.

Lee, J.E., Lee, Y.H., Kim, S.Y., Kim, Y.G., Moon, J.Y., Jeong, K.H., Lee, T.W., Ihm, C.G., Kim, S., Kim, K.H., Kim, D.K., Kim, Y.S., Kim, C.D., Park, C.W., Lee do, Y., Lee, S.H., 2016. Systematic biomarker discovery and coordinative validation for different primary nephrotic syndromes using gas chromatography-mass spectrometry. J. Chromatogr. A 1453, 105–115. https://doi.org/10.1016/j.chroma.2016.05.058.

Lee, E.M., Park, S.J., Lee, J.E., Lee, B.M., Shin, B.K., Kang, D.J., Choi, H.K., Kim, Y.S., Lee, D.Y., 2019. Highly geographical specificity of metabolomic traits among Korean domestic soybeans (Glycine max). Food Res. Int. 120, 12–18. https://doi.org/10.1016/j.foodres.2019.02.021.

Li, N., Sioutas, C., Cho, A., Schmitz, D., Misra, C., Sempf, J., Wang, M., Oberley, T., Froines, J., Nel, A., 2003. Ultrafine particulate pollutants induce oxidative stress and mitochondrial damage. Environ. Health Perspect. 111 (4), 455–460. https://doi.org/10.1289/ehp.6000.

Li, B., Tang, J., Yang, Q., Li, S., Cui, X., Li, Y., Chen, Y., Xue, W., Li, X., Zhu, F., 2017. NOREVA: normalization and evaluation of MS-based metabolomics data. Nucleic Acids Res. 45 (W1), W162–W170. https://doi.org/10.1093/nar/gkx449.

Liddelow, S.A., Guttenplan, K.A., Clarke, L.E., Bennett, F.C., Bohlen, C.J., Schirmer, L., Bennett, M.L., Munch, A.E., Chung, W.S., Peterson, T.C., Wilton, D.K., Frouin, A., Napier, B.A., Panicker, N., Kumar, M., Buckwalter, M.S., Rowitch, D.H., Dawson, V.L., Dawson, T.M., Stevens, B., Barres, B.A., 2017. Neurotoxic reactive astrocytes are induced by activated microglia. Nature 541 (7638), 481–487. https://doi.org/10.1038/nature21029.

Lim, S., Ahn, T., Lee, S., Park, S., 2017. Optical measurement of volume fraction and organic mass fraction of ultra-fine soot particles emitted from inverse diffusion flames. Fuel 210, 455–462. https://doi.org/10.1016/j.fuel.2017.08.113.

Maher, B.A., Ahmed, I.A., Karloukovski, V., MacLaren, D.A., Foulds, P.G., Allsop, D., Mann, D.M., Torres-Jardon, R., Calderon-Garciduenas, L., 2016. Magnetite pollution nanoparticles in the human brain. Proc. Natl. Acad. Sci. U. S. A. 113 (39), 10797–10801. https://doi.org/10.1073/pnas.1605941113.

Oberdorster, G., Sharp, Z., Atudorei, V., Elder, A., Gelein, R., Kreyling, W., Cox, C., 2004. Translocation of inhaled ultrafine particles to the brain. Inhal. Toxicol. 16 (6–7), 437–445. https://doi.org/10.1080/08958370490439597.

Oberdorster, G., Oberdorster, E., Oberdorster, J., 2005. Nanotoxicology: an emerging discipline evolving from studies of ultrafine particles. Environ. Health Perspect. 113 (7), 823–839. https://doi.org/10.1289/ehp.7339.

Park, S.J., Jeong, I.H., Kong, B.S., Lee, J.E., Kim, K.H., Lee, D.Y., Kim, H.J., 2016. Disease type- and status-specific alteration of CSF metabolome coordinated with clinical parameters in inflammatory demyelinating diseases of CNS. PLoS One 11 (11), e0166277. https://doi.org/10.1371/journal.pone.0166277.

Park, S.J., Kim, J.K., Kim, H.H., Yoon, B.A., Ji, D.Y., Lee, C.W., Kim, H.J., Kim, K.H., Shin, H.Y., Park, S.J., Lee, D.Y., 2019. Integrative metabolomics reveals unique metabolic traits in Guillain-Barre Syndrome and its variants. Sci. Rep. 9 (1), 1077. https://doi.org/10.1038/s41598-018-37572-w.

Poli, G., Schaur, R.J., 2000. 4-Hydroxynonenal in the pathomechanisms of oxidative stress. IUBMB Life 50 (4–5), 315–321. https://doi.org/10.1080/713803726.

Poli, G., Schaur, R.J., Siems, W.G., Leonarduzzi, G., 2008. 4-hydroxynonenal: a membrane lipid oxidation product of medicinal interest. Med. Res. Rev. 28 (4), 569–631. https://doi.org/10.1002/med.20117.

Polyzos, A.A., Lee, D.Y., Datta, R., Hauser, M., Budworth, H., Holt, A., Mihalik, S., Goldschmidt, P., Frankel, K., Trego, K., Bennett, M.J., Vockley, J., Xu, K., Gratton, E., McMurray, C.T., 2019. Metabolic reprogramming in astrocytes distinguishes region-specific neuronal susceptibility in Huntington mice. Cell Metab. 29 (6), 1258–1273 e1211. https://doi.org/10.1016/j.cmet.2019.03.004.

Rowland, H.A., Hooper, N.M., Kellett, K.A.B., 2018. Modelling sporadic Alzheimer's disease using induced pluripotent stem cells. Neurochem. Res. 43 (12), 2179–2198. https://doi.org/10.1007/s11064-018-2663-z.

Schneider, C.A., Rasband, W.S., Eliceiri, K.W., 2012. NIH image to ImageJ: 25 years of image analysis. Nat. Methods 9 (7), 671–675. https://doi.org/10.1038/nmeth.2089.

Shannon, P., Markiel, A., Ozier, O., Baliga, N.S., Wang, J.T., Ramage, D., Amin, N., Schwikowski, B., Ideker, T., 2003. Cytoscape: a software environment for integrated models of biomolecular interaction networks. Genome Res. 13 (11), 2498–2504. https://doi.org/10.1101/gr.1239303.

Shi, L., Lu, L., Harvey, G., Harvey, T., Rodriguez-Contreras, A., Alfano, R.R., 2017. Label-free fluorescence spectroscopy for detecting key biomolecules in brain tissue from a mouse model of Alzheimer's disease. Sci. Rep. 7 (1), 2599. https://doi.org/10.1038/s41598-017-02673-5.

Skogerson, K., Wohlgemuth, G., Barupal, D.K., Fiehn, O., 2011. The volatile compound BinBase mass spectral database. BMC Bioinf. 12, 321. https://doi.org/10.1186/1471-2105-12-321.

Song, Y., Li, R., Zhang, Y., Wei, J., Chen, W., Chung, C.K.A., Cai, Z., 2019. Mass spectrometry-based metabolomics reveals the mechanism of ambient fine particulate matter and its components on energy metabolic reprogramming in BEAS-2B cells. Sci. Total Environ. 651 (Pt 2), 3139–3150. https://doi.org/10.1016/j.scitotenv.2018.10.171.

Sutherland, G.T., Chami, B., Youssef, P., Witting, P.K., 2013. Oxidative stress in Alzheimer's disease: primary villain or physiological by-product? Redox Rep. 18 (4), 134–141. https://doi.org/10.1179/1351000213Y.0000000052.

Tarkowski, E., Andreasen, N., Tarkowski, A., Blennow, K., 2003. Intrathecal inflammation precedes development of Alzheimer's disease. J. Neurol. Neurosurg. Psychiatry 74 (9), 1200–1205. https://doi.org/10.1136/jnnp.74.9.1200.

Toledo, J.B., Arnold, M., Kastenmuller, G., Chang, R., Baillie, R.A., Han, X., Thambisetty, M., Tenenbaum, J.D., Suhre, K., Thompson, J.W., John-Williams, L.S., MahmoudianDehkordi, S., Rotroff, D.M., Jack, J.R., Motsinger-Reif, A., Risacher, S.L., Blach, C., Lucas, J.E., Massaro, T., Louie, G., Zhu, H., Dallmann, G., Klavins, K., Koal, T., Kim, S., Nho, K., Shen, L., Casanova, R., Varma, S., Legido-Quigley, C., Moseley, M.A., Zhu, K., Henrion, M.Y.R., van der Lee, S.J., Harms, A.C., Demirkan, A., Hankemeier, T., van Duijn, C.M., Trojanowski, J.Q., Shaw, L.M., Saykin, A.J., Weiner, M.W., Doraiswamy, P.M., Kaddurah-Daouk, R., Alzheimer's Disease Neuroimaging, I, the Alzheimer Disease Metabolomics, C, 2017. Metabolic network failures in Alzheimer's disease: a biochemical road map. Alzheimers Dement. 13 (9), 965–984. https://doi.org/10.1016/j.jalz.2017.01.020.

Usuda, K., Kawase, T., Shigeno, Y., Fukuzawa, S., Fujii, K., Zhang, H., Tsukahara, T., Tomonaga, S., Watanabe, G., Jin, W., Nagaoka, K., 2018. Hippocampal metabolism of amino acids by L-amino acid oxidase is involved in fear learning and memory. Sci. Rep. 8 (1), 11073. https://doi.org/10.1038/s41598-018-28885-x.

Vassalli, P., 1992. The pathophysiology of tumor necrosis factors. Annu. Rev. Immunol. 10, 411–452. https://doi.org/10.1146/annurev.iy.10.040192.002211.

Vlassenko, A.G., Vaishnavi, S.N., Couture, L., Sacco, D., Shannon, B.J., Mach, R.H., Morris, J.C., Raichle, M.E., Mintun, M.A., 2010. Spatial correlation between brain aerobic glycolysis and amyloid-beta (Abeta) deposition. Proc. Natl. Acad. Sci. U. S. A. 107 (41), 17763–17767. https://doi.org/10.1073/pnas.1010461107.

Wang, R., Li, J.J., Diao, S., Kwak, Y.D., Liu, L., Zhi, L., Bueler, H., Bhat, N.R., Williams, R.W., Park, E.A., Liao, F.F., 2013. Metabolic stress modulates Alzheimer's beta-secretase gene transcription via SIRT1-PPARgamma-PGC-1 in neurons. Cell Metab. 17 (5), 685–694. https://doi.org/10.1016/j.cmet.2013.03.016.

Wang, X., Jiang, S., Liu, Y., Du, X., Zhang, W., Zhang, J., Shen, H., 2017. Comprehensive pulmonary metabolome responses to intratracheal instillation of airborne fine particulate matter in rats. Sci. Total Environ. 592, 41–50. https://doi.org/10.1016/j.scitotenv.2017.03.064.

Xu, J., Begley, P., Church, S.J., Patassini, S., Hollywood, K.A., Jullig, M., Curtis, M.A., Waldvogel, H.J., Faull, R.L., Unwin, R.D., Cooper, G.J., 2016. Graded perturbations of metabolism in multiple regions of human brain in Alzheimer's disease: snapshot of a pervasive metabolic disorder. Biochim. Biophys. Acta 1862 (6), 1084–1092. https://doi.org/10.1016/j.bbadis.2016.03.001.

Zhang, C., Rodriguez, C., Spaulding, J., Aw, T.Y., Feng, J., 2012. Age-dependent and tissue-related glutathione redox status in a mouse model of Alzheimer's disease. J. Alzheimers Dis. 28 (3), 655–666. https://doi.org/10.3233/JAD-2011-111244.

Zhang, Y., Hu, H., Shi, Y., Yang, X., Cao, L., Wu, J., Asweto, C.O., Feng, L., Duan, J., Sun, Z., 2017. (1)H NMR-based metabolomics study on repeat dose toxicity of fine particulate matter in rats after intratracheal instillation. Sci. Total Environ. 589, 212–221. https://doi.org/10.1016/j.scitotenv.2017.02.149.

Zhong, J., Karlsson, O., Wang, G., Li, J., Guo, Y., Lin, X., Zemplenyi, M., Sanchez-Guerra, M., Trevisi, L., Urch, B., Speck, M., Liang, L., Coull, B.A., Koutrakis, P., Silverman, F., Gold, D.R., Wu, T., Baccarelli, A.A., 2017a. B vitamins attenuate the epigenetic effects of ambient fine particles in a pilot human intervention trial. Proc. Natl. Acad. Sci. U. S. A. 114 (13), 3503–3508. https://doi.org/10.1073/pnas.1618545114.

Zhong, J., Trevisi, L., Urch, B., Lin, X., Speck, M., Coull, B.A., Liss, G., Thompson, A., Wu, S., Wilson, A., Koutrakis, P., Silverman, F., Gold, D.R., Baccarelli, A.A., 2017b. B-vitamin supplementation mitigates effects of fine particles on cardiac autonomic dysfunction and inflammation: a pilot human intervention trial. Sci. Rep. 7, 45322. https://doi.org/10.1038/srep45322.